All-dielectric Huygens' meta-waveguides for resonant integrated photonics

Sırmacı, Yunus Denizhan; Barreda Gomez, Angela; Pertsch, Thomas; Schmid, Jens H.; Cheben, Pavel; Staude, Isabelle

Publisher's version / Version de l'éditeur:
https://doi.org/10.1002/lpor.202200860
Laser & Photonics Reviews, 17, 6, 2023-06

LASER & PHOTONICS REVIEWS
www.lpr-journal.org

All-Dielectric Huygens' Meta-Waveguides for Resonant Integrated Photonics

Yunus Denizhan Sırmacı, Angela Barreda Gomez, Thomas Pertsch, Jens H. Schmid, Pavel Cheben, and Isabelle Staude**

The growing maturity of nanofabrication technology has recently enabled the deployment of high-quality subwavelength nanostructures on photonic chips. Combining existing photonic waveguide technology with the paradigms adapted from metamaterials opens new avenues towards unprecedented control of guided light waves. However, developing new functionalities while preserving efficiencies and offering compatibility with current technology remains a major challenge in on-chip nanophotonics. Here, a novel silicon nanophotonic waveguide comprising a chain of resonantly forward scattering nanoparticles empowered by spectrally overlapping electric and magnetic dipolar Mie-type resonances is proposed and demonstrated. The propagation loss of the meta-waveguides in the telecom spectral range is as low as 0.4 dB mm^{-1}, exceeding the current record for Mie-resonant waveguides by more than an order of magnitude. Furthermore, the meta-waveguides support a negative group index over a broad spectral range of 60 nm and regions of vanishing and anomalous dispersion within the transmission band. Finally, it is shown that meta-waveguide topologies can implement compact resonance-protected waveguide bends and efficient splitters within just 320 nm propagation length. This work addresses the fundamental challenges of miniaturization, dispersion, and scattering control in integrated photonics and opens new opportunities for enhancing light–matter interactions, interfacing nanophotonic components, and developing nonlinear, ultrafast, and quantum optics resonant on-chip devices.

1. Introduction

As the ever-higher integration density of electronic circuits reaches its limits in terms of bandwidth and power density, photonic integrated solutions are emerging as a promising route toward ultrafast and broadband information processing with low power consumption.[1,2,3] Huge progress has been achieved in the realization of wafer-scale integrated photonics during the last decade, showing an exponential increase in the number of photonic components that can be integrated on an optical chip.[4] This development offers tremendous opportunities in important emerging application areas such as photonic quantum computing,[4] on-chip optical signal processing,[5] neuromorphic computing and artificial intelligence,[6] sensing,[7] and classical and quantum communications.[8]

However, the functional scope, performance and integration density of state-of-the-art photonic integrated circuits are currently limited by the fundamental properties of their essential building blocks, including optical waveguides. As such, there is a high demand for novel waveguiding structures which can reduce device footprints and at the same time empower more complex device functions beyond mere waveguiding, all of which needs to be realized in a complementary metal-oxide-semiconductor (CMOS) compatible way.[9]

Nanophotonics offers new pathways for light manipulation at the nanoscale. Various concepts have been explored regarding its potential for efficient manipulation and guiding of light waves on a photonic chip.[10] Initially, most research in this direction concentrated on photonic crystal slab waveguides, which offer interesting opportunities regarding miniaturization and light–matter interaction enhancement. However, especially for low-group-velocity designs, realistic fabricated structures turned out to be severely hampered by backscattering losses.[11] Subsequently, subwavelength grating (SWG) metamaterial waveguides[12–15] were developed as a powerful tool for overcoming performance limitations of conventional dielectric waveguides. Later on, in the wake of research on optical metamaterials[16] and metasurfaces,[17] i.e., artificial structures with engineered optical properties beyond those attainable by

Y. D. Sırmacı, A. Barreda Gomez, I. Staude
Friedrich-Schiller-University Jena
Institute of Solid State Physics
07743 Jena, Germany
E-mail: yunus.denizhan.sirmaci@uni-jena.de;
isabelle.staude@uni-jena.de

Y. D. Sırmacı, A. Barreda Gomez, T. Pertsch, I. Staude
Friedrich-Schiller-University Jena
Institute of Applied Physics
Abbe Center of Photonics
07745 Jena, Germany

J. H. Schmid, P. Cheben
National Research Council of Canada
Ottawa, Ontario K1A 0R6, Canada

The ORCID identification number(s) for the author(s) of this article can be found under https://doi.org/10.1002/lpor.202200860

DOI: 10.1002/lpor.202200860

natural materials, different metamaterial-inspired waveguiding concepts,[10] recently termed meta-waveguides,[9] have been explored. Among these meta-waveguides, nanoplasmonic implementations offer unprecedented miniaturization and optical field concentration but typically suffer from high absorption losses, dramatically reducing propagation lengths to the micrometer range.[18] As a possible workaround, the local hybridization of conventional on-chip waveguides with plasmonic elements was also suggested.[19] However, the problem of absorption losses in plasmonic structures is only reduced, not mitigated, by this approach, and the demonstrated functionalities and performance gains of such devices remain limited. All-dielectric structures, on the other hand, can exhibit very low propagation losses. While nanostructuring on a subwavelength scale has been extensively used to engineer the effective optical properties of SWG waveguides,[12–14,20,21] these structures operate in an off-resonant, effective-medium regime, while some of the most intriguing effects and functionalities of metamaterials require the excitation of tailored resonances at nanoscale.[22,23]

More recently, Mie-resonant all-dielectric nanoparticles were explored as alternative building blocks for on-chip optical meta-waveguides. Following years of plasmonics-dominated research in optical metamaterials and metasurfaces, such high-refractive-index nanoresonators have already revolutionized the field of optical metasurfaces, particularly regarding device efficiency and functional scope.[10] Numerous related applications have been pursed, including lensing,[24] information and image processing,[25] machine learning,[26] quantum state detection,[27] lidar,[28] lasing,[29] photonic displays,[30] quantum light sources,[31] and spectroscopy,[32] to name a few. The great application potential of all-dielectric metasurfaces leverages the favorable properties of the constituent nanoresonators, in particular their low absorption losses and the ample engineering options offered by their electric and magnetic multipolar response and various field coupling phenomena.

The possibility of guiding light at the nanoscale by means of all-dielectric nanoparticle arrays has been previously explored, starting with subwavelength grating arrays.[12–14,20] Earlier investigations also concentrated on theoretical or numerical studies[33–35] as well as proof-of-principle demonstrations in the microwave spectral range.[35–37] These works already demonstrated the prospect of superior guiding performance of dielectric nanoparticle chains compared to plasmonic structures,[33,36] slow-light waveguiding,[34] as well as the guiding of light around sharp corners,[35] side-coupled resonators,[37] and splitters.[33] Also, the importance of simultaneous electric and magnetic response of the nanoparticles for achieving a negative group velocity[38] and of resonance engineering to enhance the transmittance through bends[35] was pointed out. The first experimental demonstration in the optical spectral range was presented in 2017 by Bakker et al.,[39] achieving waveguiding over distances beyond 500 μm at $\lambda = 960$ nm in chains of silicon cylinders exhibiting coupled magnetic dipole resonances. However, with a minimum value of 5.5 dB mm^{-1}, losses were relatively high. Chains of Mie-resonant dielectric nanoparticles have furthermore shown their potential for building nanolasers,[40] for nonlinear photonics[38] or for dielectric nanoantennas with a high Purcell factor.[22,41]

Here we propose and experimentally demonstrate a new type of fully CMOS-compatible on-chip optical meta-waveguide operating in the telecom spectral range, comprising a chain of silicon nanoresonators engineered to exhibit nearly exclusively forward-scattering properties. This is achieved by spectrally overlapping the electric and magnetic dipolar Mie-type resonances over their full resonance width via a judicious choice of the nanoresonator geometry. As exploited in high-transmittance all-dielectric Huygens' metasurfaces,[42] backscattering from such nanoresonators is strongly suppressed enforcing the first Kerker condition of zero backward scattering[43] over the entire bandwidth of their Mie-resonant response, thus operating in the Huygens' regime. The fabricated waveguides have lengths of up to several millimeters and show transmission losses as low as 0.4 dB mm^{-1}, exceeding the current record for Mie-resonant waveguides by more than an order of magnitude. The achieved losses are comparable with those of SWG waveguides, while offering many new design degrees of freedom and opportunities based on resonant light–matter interaction.[21] Remarkably, due to the broadband electric and magnetic response of its building blocks, our resonant waveguides exhibit negligible back-scattering even from very strong perturbations. This is an unprecedented characteristic for integrated photonic waveguides. Additionally, they feature a negative group index over their full operation bandwidth and over propagation distances of several millimeters, as well as regions of vanishing and anomalous dispersion within the transmittance band. Finally, as exemplary basic waveguide components, we also demonstrate resonant-protected bend topologies, reaching bend radii down to 2.7 μm, as well as efficient ultracompact resonant splitters. Altogether, this work adds many new complementary opportunities to the toolbox of integrated photonics. Owing to the competitive efficiency of the demonstrated waveguide structures in combination with their resonant optical response, negligible back reflection, and natural compatibility with nanophotonic components, Huygens' waveguides may potentially enable a range of new device functionalities in the areas of complex on-chip components, dispersion management, integrated quantum optics, sensing, as well as nonlinear and ultrafast integrated photonics.

2. Results

As a first step in the design process of the Huygens' meta-waveguides, we optimized a single Mie-resonant high-refractive-index nanoparticle (NP) to exhibit strongly forward scattering properties in the telecom spectral range. Specifically, we considered a silicon nanocuboid (see **Figure 1**a) with a fixed height of 220 nm embedded in a silica matrix and optimized its electric and magnetic response by adjusting the NP width-to-length aspect ratio. Single crystal silicon was chosen as NP material due to its high refractive index, low losses in the near-infrared, and widespread technological use in CMOS electronics and silicon photonics. The height of the NP is kept fixed to ensure compatibility with standard silicon-on-insulator (SOI) wafer fabrication technology widely accessible through silicon photonic foundry offerings. We determined the optimal NP size to be $l = 315$ nm, $w = 515$ nm and $h = 220$ nm (see Figure 1a), for TE polarization (E-field parallel to the y-axis). Figure 1b shows the calculated

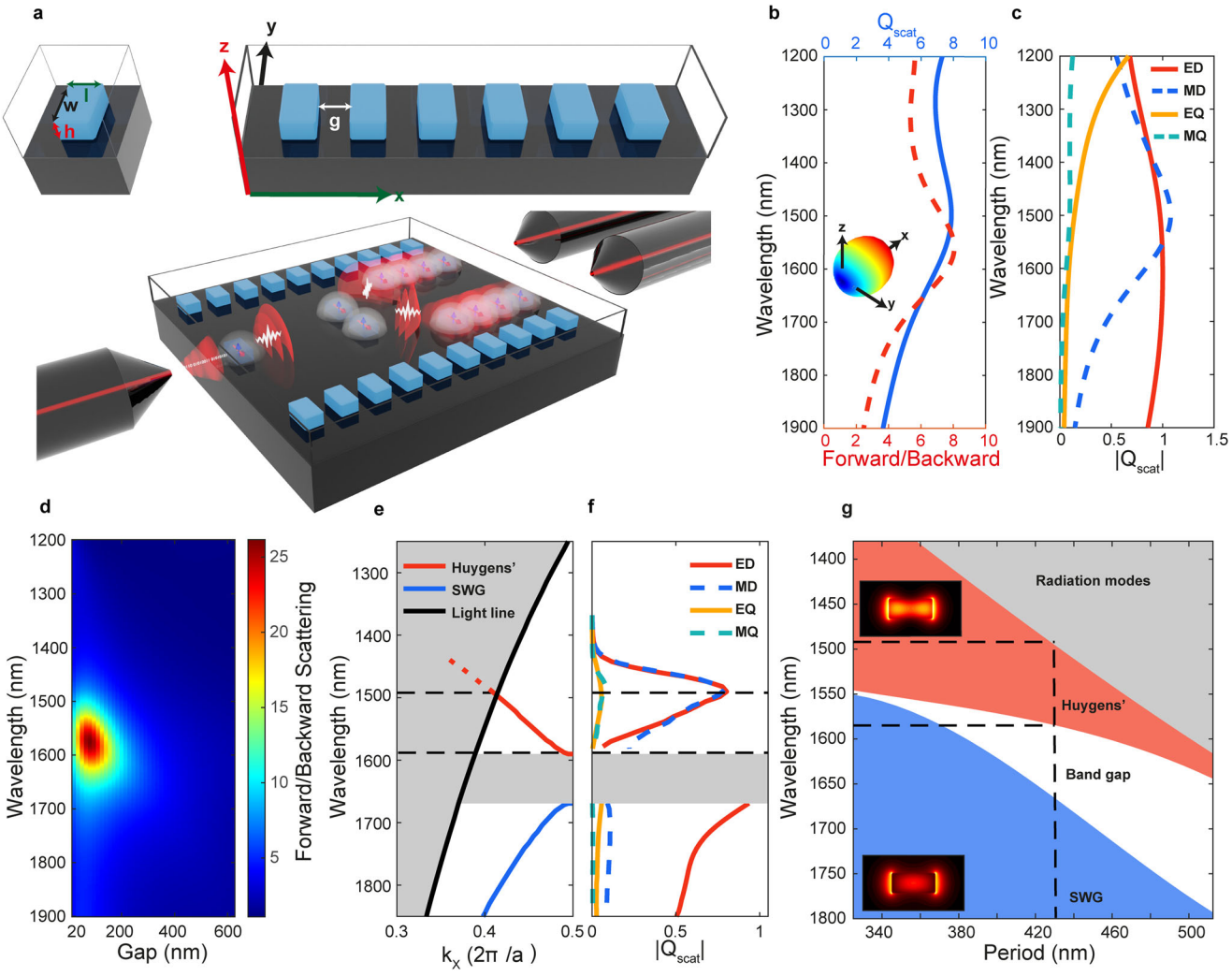

Figure 1. From isolated Huygens' scatterers to resonant meta-waveguides. a) Schematic of single-isolated silicon NP (l = 315 nm, w = 515 nm, h = 220 nm, embedded in a silica layer forming the upper and lower waveguide cladding (top left, the silicon substrate is not shown). Schematic of a Huygens' waveguide (g = 115 nm) composed of the described NPs (top right) and schematic representation of an envisioned NP-based photonic integrated circuit (bottom). b) Scattering cross-section (blue) and forward-to-backward scattering ratio (red) of a single isolated NP. c) Multipolar decomposition of single nanoantenna (described in (a)). d) Forward-to-backward scattering ratio of a dimer as a function of gap size g. e) Dispersion diagram of an infinite NP chain for g = 115 nm. f) Multipolar decomposition of the fields of an infinite array with the structural parameters as in (e). g) Band diagram of 1D array as a function of structural period for k_x = 0.5 ($2\pi/a$).

scattering-cross section (blue) of the optimized NP as well as its forward-to-backward scattering ratio (FBR, in red), which reaches its optimum around 1550 nm, close to the scattering maximum. We also confirmed directional scattering by calculating the far-field scattering pattern of the designed NP at λ = 1550 nm (Figure 1b, inset).

To understand the observed directionality properties, we performed a Cartesian multipolar decomposition. The unidirectional forward scattering is due to the excitation of in-phase electric dipole (ED) and magnetic dipole (MD) resonances with their respective moments p and m approximately fulfilling the first Kerker condition[43,44] ($p - \frac{\sqrt{\epsilon_r} m}{c} = 0$, where ϵ_r is the relative permittivity of the medium and c is the speed of light; vanishing electric quadrupole moment is assumed) over the entire resonance bandwidth. This type of NPs are commonly referred to as Huygens' scatterers.[42] Figure 1c shows the multipolar decomposition of the scattered fields (see Experimental Section), normalized to the maximum of the ED contribution. For the designed NP of Figure 1a, the ED moment (red) exhibits a low quality factor resonance with almost constant magnitude throughout the spectrum of interest, while the MD moment (blue dashed) peaks near 1520 nm with a moderately higher quality factor. We observe ED and MD moments of comparable magnitudes over a wide spectral range (1300–1600 nm). Equal values are reached near 1380 and 1551 nm wavelengths. The quadrupole moments are weak at the long-wavelength side and start to emerge at shorter wavelengths. Thus, while the total scattering cross section is strongly dominated by ED and MD moments at 1550 nm, there is a more

significant electric quadrupole (EQ) contribution at 1380 nm. This explains why a larger FBR is observed near 1550 nm.

Next, we considered a dimer composed of two Huygens NPs and studied its directional scattering efficiency as a function of the size of the gap between them. To this end, we calculated the FBR for different gap sizes from 20 to 620 nm in 10 nm steps. Figure 1d shows the FBR, which peaks around 1570 nm, slightly redshifted with respect to the FBR maximum observed for the individual NP. For very small gap sizes (<50 nm), we observe lower forward scattering efficiencies, likely due to the coupling effects that perturb the multipolar interference of the overall structure. For large gap sizes (>180 nm), the FBR also decreases as the scattered field from the first NP starts to delocalize due to the finite directivity (Figure 1b inset) of the individual NP. We observe high FBRs up to 25 for gap sizes between 80–140 nm in the region from 1520 to 1620 nm. In this regime, the fields of the NPs are sufficiently decoupled to maintain fundamental scattering properties of the individual particles, yet the NPs are in close enough proximity so that the second NP tends to effectively refocus the light scattered from the first NP. This can be interpreted as a waveguiding effect along the dimer.

Up to now, we considered the scattering properties of isolated NPs and dimers but waveguiding on a chip requires many particles arrayed along the propagation direction. Therefore, we calculated the dispersion of an infinite NP array for a gap size g of 115 nm, corresponding to a lattice period of 430 nm. These results are shown in Figure 1e. We observe two guided modes, separated by the photonic band gap (PBG) of the system. The light line of SiO_2 is shown in black and the continuum of leaky modes and PBG regions are shaded grey. The fundamental guided TE mode (blue) primarily resides in the long-wavelength region, where the structure sizes are considerably smaller than the wavelength of propagating light and reaches up to the PBG at the edge of the Brillouin zone, where the array period equals half the effective wavelength. In the long wavelength limit, the behavior of this mode can be described by expressing the effective material refractive index as a weighted average of the constituent refractive indices. This region is harnessed for subwavelength grating waveguides,[12–14,20] and we refer to it as SWG band. The second guided mode (red) is spectrally positioned above the PBG in the vicinity of the Huygens' NPs resonance wavelength, hence we call it the Huygens' band. For the chosen period, the Huygens' band is situated in the telecommunication wavelength range (horizontal dashed lines). In order to gain further insight into the mode properties of these two different branches, we perform a multipolar decomposition of the fields excited inside the individual NPs for the 1D periodic array. To this end, we calculate the Bloch modes for a discrete set of wavevectors in normalized k_x range from 0.3 to 0.5 ($2\pi/a$) and perform a multipole analysis at the unit cell level (see Experimental Section). These results are represented in Figure 1f. We normalize the different multipole contributions to the maximum of the ED contribution. As expected from Rayleigh theory,[45] the ED response dominates the scattered field in the long-wavelength regime, and we can clearly observe this behavior for the SWG mode. Most importantly, the multipole decomposition for the Huygens' band reveals that the Kerker condition of matching electric and magnetic dipolar moments is fulfilled over the entire bandwidth. Interestingly, not only the electric and magnetic dipolar contributions overlap almost perfectly, but corresponding quadrupolar orders also show a near-ideal overlap. As such, the coupling in the array preserves the resonant properties of the individual NPs and leads to a locking of the relative magnitudes of the electric and magnetic moments so that the NPs in the array can be regarded as coupled Huygens' scatterers over a wide spectral range of ≈100 nm.

To study the influence of the NP spacing on the waveguide dispersion, we varied the gap size g from 0 to 200 nm, corresponding to lattice periods of 315–515 nm. Our calculation results are summarized in Figure 1g, showing that the bandwidth of the Huygens' band decreases as the gap between the NPs increases. This trend can be explained by the transition of Huygens' mode into a continuum of leaky modes as the light line is crossed (gray shaded area). In fact, when we compare the behavior of the dimer (Figure 1c) and infinite array (Figure 1g) as a function of gap size, we see good correspondence in the spectral position of the FBR maximum and that of the Huygens' band, respectively. We also calculated the field profiles of the Bloch modes ($|E|^2$ from the middle of y–z cross section of the particle) of each branch at $k_x = 0.425$ for a period of 430 nm. The results are shown as insets in Figure 1g. Note that, the modal field profile of the SWG branch resembles the fundamental (TE_0) mode of a wire waveguides, as expected, while Huygens' branch shows two maxima inside the particle (resembling TE_1 mode of a wire waveguide) due to the localized field circulation. Finally, we compared the Bloch mode of the infinite 1D array for a wavelength of 1550 nm, corresponding to $k_x = 0.455$, with the eigenstate of a single isolated NP. The field profiles are almost identical (Figure S1, Supporting Information), demonstrating that single-particle resonance properties are well preserved in infinite arrays. These results confirm that arrays of Mie resonant Huygens' scatterers provide a new type of guiding mechanism in integrated photonics, where waveguiding is enhanced by highly directional forward scattering properties of carefully engineered individual NPs.

3. Experimental Demonstration

In order to investigate the properties and guiding performance of the Huygens' meta-waveguides experimentally, the designed structures were fabricated using electron-beam lithography on a silicon-on-insulator platform, followed by plasma etching (see Experimental Section). The SOI wafer consists of a 220-nm-thick single crystal silicon layer, which is separated from the silicon handle wafer by a 3-μm-thick buried oxide (SiO_2) layer. A 3-μm SiO_2 layer is deposited as an upper cladding to homogeneously cover the waveguide core after etching. The entire fabrication process was performed by a commercial silicon photonics foundry service (Applied Nanotools Inc.), demonstrating the compatibility of our design with industrial processes. A typical fabricated structure before depositing SiO_2 cladding is shown in **Figure 2**a. In order to systematically study the loss of the Huygens' meta-waveguide, a set of test waveguides of different lengths was fabricated on a single chip (see Experimental Section). An adiabatic mode converter was used to efficiently couple light into the resonant mode of the Huygens' meta-waveguides from the fundamental mode of conventional 450-nm-wide silicon strip waveguides. The mode converter loss was determined as 0.35 ± 0.25 dB in an independent measurement using a series of couplers (up to 16) connected back-to-back. The low intrinsic cou-

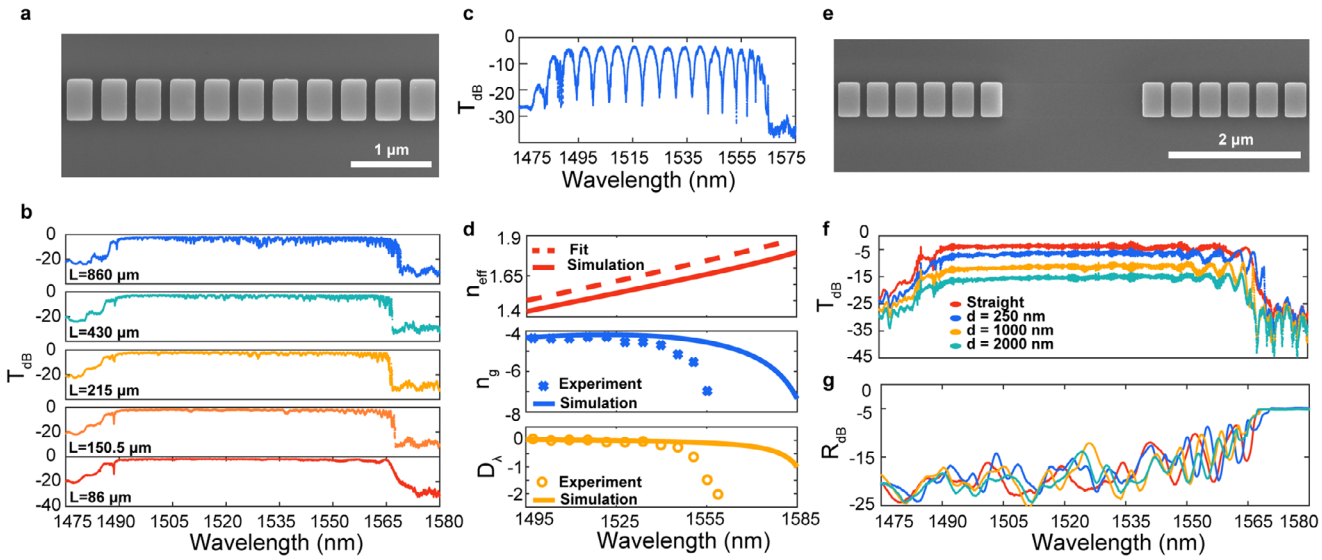

Figure 2. Experimental characterization of Huygens' meta-waveguides. a) Top view scanning-electron microscope (SEM) image of a fabricated Huygens' meta-waveguide. b) Experimental transmittance spectra of Huygens' meta-waveguides with different lengths. c) Measured transmittance of a Mach–Zehnder interferometer with arms comprising Huygens' meta-waveguides. The geometrical path difference between the arms is 86.13 μm. d) Simulated and experimentally fitted effective index n_{eff}, group index n_g, and group velocity dispersion parameter of the Huygens' meta-waveguide. e) SEM image of an exemplary disrupted Huygens' meta-waveguide. f) Measured transmittance and g) reflectance spectra of disrupted Huygens' meta-waveguides with different disruption length (d).

pler loss is important as it allows a seamless integration of silicon strip waveguides and Huygens' meta-waveguides in an integrated photonic circuit. Finally, for highly efficient and broadband coupling from a lensed fiber to the interconnecting strip waveguides, metamaterial edge couplers were formed near the chip facets as described in ref. [46]. The measured fiber-chip coupling loss was ≈1.1 dB per facet over the wavelength range of 1490–1580 nm.

Waveguide transmission measurements were performed using our in-house optical characterization bench (see Experimental Section). We determined the mode propagation loss of Huygens' waveguides by the cut-back technique using straight waveguides of different lengths ranging from 86 μm to 0.86 mm, comprising 200 to 2000 Huygens' scatterers. Figure 2b shows the transmittance spectra of several Huygens' meta-waveguides with nominal structural parameters identical to those used in the FDTD simulations (Figure 1a). We normalized all spectra with respect to the reference loss of the optical setup (see Experimental Section). Within the spectral range of our characterization setup, the Huygens' band is clearly observed between the light line of the SiO_2 cladding at 1490 nm and the PBG edge near 1570 nm. For sufficiently long waveguides, we observe an abrupt transition from high transmission to high reflection. The waveguide propagation loss only slightly increases when approaching the PBG region, while a smooth transition is observed above the light line as the leaky waves gradually build up. Compared with the FDTD simulations (Figure 1e), we observe a small (≈10 nm) blue shift in the PBG edge, which we attribute to fabrication bias. To further refine our loss analysis, we characterized five additional Huygens' meta-waveguides with a maximum length of 7.78 mm. For each wavelength, we line fitted the losses as a function of the waveguide length, yielding a propagation loss of 0.4–1 dB mm^{-1} within the Huygens passband range of 1490–1570 nm. This is the first time that such an extended array of coupled resonators comprising up to 18 000 coupled Mie-resonant NPs is reported, with the measured loss value unprecedented for resonant arrays and comparable to conventional SWG waveguides.[13] While earlier work[47] reported slightly lower losses, note that the silicon NP chains investigated in there operate in the subwavelength regime below the band gap thus are fundamentally SWG waveguides,[14] unlike our NP chains operating above the band gap. Theoretically, our Huygens' meta-waveguides, which are operating below the light line, can guide light without any radiation losses. We attribute the observed propagation loss to fabrication imperfections, which cause scattering and perturb the periodicity of the waveguide, thus resulting in coupling of guided light to radiation modes.

In order to determine the group index ($n_g = n + \omega dn/d\omega$) of the Huygens' meta-waveguides, we designed and fabricated an unbalanced Mach-Zehnder interferometer (MZI) with the arms incorporating Huygens' meta-waveguides with path difference of 86 μm. The measured transmittance spectrum of the MZI is shown in Figure 2c, exhibiting a high extinction ratio. We calculated the group index (see Figure 2d) based on the free spectral range (FSR) of the transmission dips using the relation $\Delta\lambda_{\mathrm{FSR}} = \frac{c}{n_g L}$ (where c is the speed of the light in the vacuum, n_g is the group index, and L is the geometrical path difference between the MZI arms). The experimental transmittance spectrum was fitted to the transfer function of the MZI by expanding the effective index up to the third order of the Taylor series.[48] This method allows to retrieve both the average absolute value of the group index and its sign. Figure 2d also shows the fitted effective index of the waveguide. In comparison to the theoretical value (by using Figure 1e), the measurement yields a slightly higher effective index, which is consistent with the blueshift of the PBG edge due to fabrication bias. For the fabricated Huygens' meta-

waveguides, this method yields a negative group index with an average value of −4.65 across the Huygens' band. Away from the PBG, the group index shows a weak dependence on wavelength, while it decreases to about −7.5 as the PBG edge (1585 nm) is approached. For comparison with theoretical predictions, we also calculated the group index from the dispersion diagram (see Figure 1e). The results are shown in Figure 2d alongside the experimental data, with a good overall agreement between the theoretical and measured values. We merely observe some minor discrepancies on the longer wavelength side, related to the aforementioned blue shift of the PBG.

Negative values of the group index can be achieved in lossy media,[49,50,51] where the dispersion properties are controlled by either material selection or locally structured resonances over a narrow spectral range, as well as in 1D photonic crystals.[38] Our Huygens' meta waveguides exhibit a negative group index over a large bandwidth of about 60 nm, in combination with very low losses and large propagation distances. Furthermore, the group velocity dispersion parameter $D_\lambda = \frac{\partial}{\partial\lambda}\frac{1}{v_g}$ transitions from close to zero to negative values as the band gap is approached, corresponding to regions of almost vanishing to negative group velocity dispersion. They offer interesting new opportunities, e.g., for compensating the broadening of short laser pulses during propagation in on-chip waveguides, which is of major importance in on-chip nonlinear and quantum optics.

Next, we investigate the ability of our Huygens' meta-waveguides to suppress backscattering effects. This fundamental property is expected from the spectrally overlapping electric and magnetic dipole moments in the individual scatterers, causing them to radiate preferentially in the forward direction while the backward radiation is dramatically reduced. In order to quantify this effect, we introduced local perturbations in our meta-waveguides by removing several Huygens' scatterers from the array. First, we performed FDTD simulations of perturbed waveguides consisting of 50 NP. The transmittance was observed to drop compared to an unperturbed waveguide from 99% to 21.5% (−6.6 dB) when a 1 μm gap was introduced in the middle of the array. However, reflection remained practically negligible and virtually unaffected at ≈0.03%. This is completely different behavior compared to any previously known waveguide mechanisms, including photonic band gap and index guiding. This mitigation of backward scattering, while it appears to contradict generally accepted notions in waveguide engineering, is a rigorous consequence of the Kerker effect. Note that, the light returned backward from any reflection channels, such as defects in the other parts of the chip, will also propagate with suppressed backscattering as the system is reciprocal and propagation in both directions is allowed. To demonstrate this intriguing phenomenon experimentally, we fabricated several Huygens' waveguides with a local refractive index discontinuity by introducing gaps of different lengths, i.e., 250 nm, 1 μm, and 2 μm. Figure 2e shows an SEM micrograph of a fabricated resonant waveguide with a 2-μm-long gap. We measured both the transmittance and reflectance of these three discontinued waveguides, employing a fiber optic circulator to determine the reflected power. According to the measurements shown in Figure 2f, there is 7.4 dB penalty in transmittance for a discontinued structure with a 1 μm gap compared to continuous waveguide at 1525 nm, which is consistent with the theoretically expected field radiation leakage. However, in reflectance, introducing perturbations by any of the considered gap sizes does not introduce any notable increase in reflected power, as shown in Figure 2g. Note that, the overall reflectance is limited by the performance of the entire test structure, including the chip facet, the edge couplers, the interconnecting waveguides, and the mode transformers. The observed behavior is fundamentally different compared to other types of waveguides, including strip, SWG and photonic crystal waveguides. We have demonstrated a range of appealing and unique properties of Huygens' meta-waveguides that have no parallel in integrated photonics. In the following, we will investigate their capability to implement exemplary conventional on-chip components, namely waveguide bends and power splitters. To investigate the resonant guiding of light around sharp corners, we designed and fabricated several arrays of Huygens' scatterers forming 90° bends with different radii. In the most compact implementation, we use an array of 10 trapezoidal scatterers with the same volume as the cuboids, arranged along an arc with a minimum bend radius of 2.7 μm. To systematically measure waveguide bend losses, we fabricated 4 sets of test structures, each comprising waveguides with 4, 8, 16, and 20 bends folded in a serpentine pattern, as shown in **Figure 3**a. Each set contains 6 different bend radii, r = 2.7, 3.8, 5.4, 7.6, 10.3, and 21 μm (shown in Figure 3c). For measurements taken at different wavelengths, we line fitted the losses as a function of number of bends and calculated the bend loss for different bend radii. In Figure 3b, the measured bend loss is shown as a function of bend radius for a wavelength of 1525 nm near the resonance peak.

To compare our experimental results with theory, we also simulated light propagation through the bends to determine the mode propagation loss. To this end, we calculated the Floquet–Bloch mode of the infinite NP array at 1525 nm and $k_x = 0.425$ and used it as an excitation source. We estimated the mode propagation loss along the bend by placing power monitors in the middle of each segment. These results are shown in Figure 3b together with experimental values, yielding a good overall agreement. The inset of Figure 3a shows the simulated electric-field intensity profile in a bend with a radius of 2.7 μm, yielding a calculated/measured transmittance of 97.5%/94.2%. For a bend radius of 3.8 μm, the measured transmittance was 97.9%. We furthermore checked that for each trapezoidal scatterer the Kerker condition is still satisfied as the scatterers' orientation changes along the bend. In order to compare the performance of the Huygens' meta-bends with conventional bends, we estimated the bend loss for index-equivalent non-resonant waveguides, including an SWG waveguide structure and a conventional waveguide with the same effective index as the Huygens' waveguide. We found that the minimum bend radius for these equivalent non-resonant waveguides is about 8 μm, while no index guiding was observed for bending radii under 7.6 μm, for which the Huygens' meta-bends still show a high transmission. It is important to remark that these compact bend radii are achieved with a simple circular bend arc. The performance of our design can likely be improved by employing Bezier or Euler bend curvatures.[52] These results confirm that the Mie resonances of the individual scatterers have a protecting effect on the guiding mechanism in the waveguide.

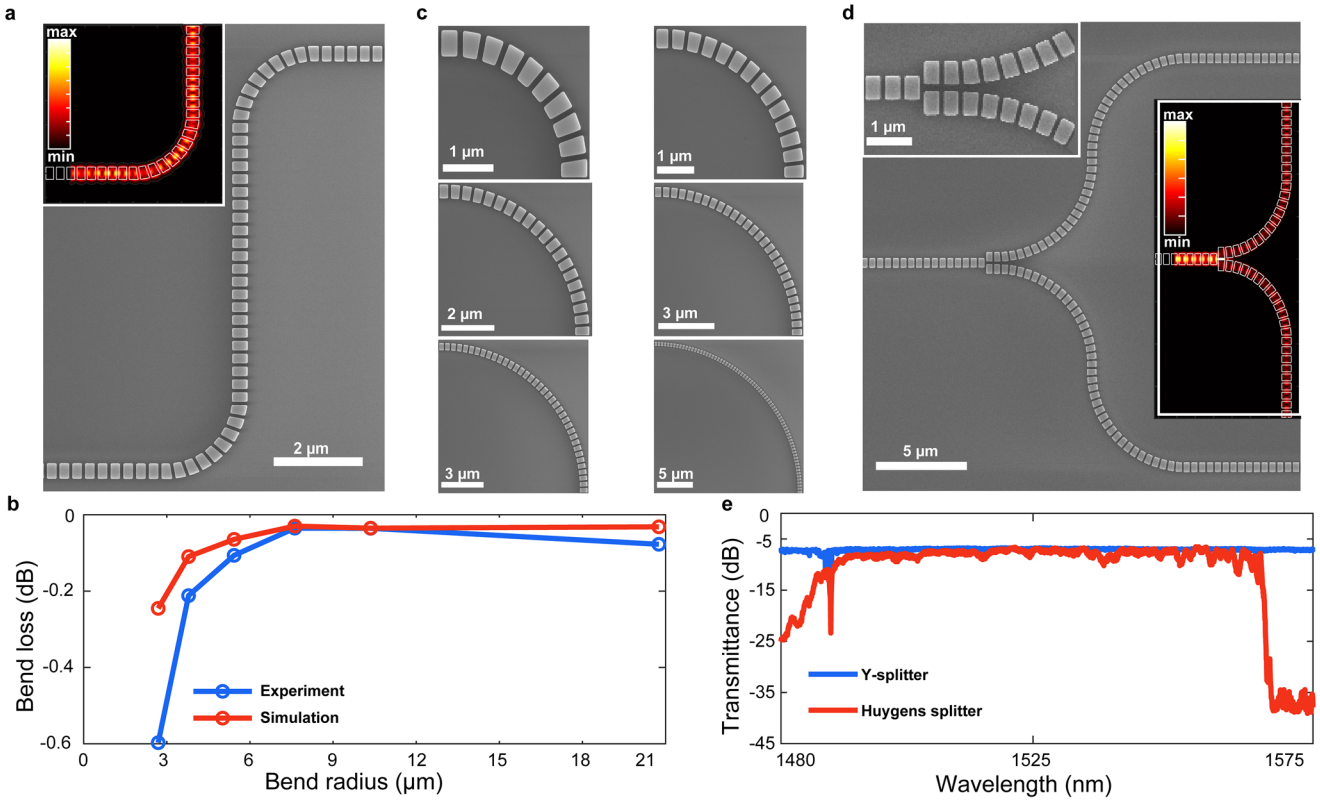

Figure 3. Waveguide bends and power splitters based on Huygens' scatterers. a) SEM image of two consecutive 10-NP-long 90° Huygens' meta-waveguide bends connected by a straight waveguide section of 20 NPs. The inset displays the corresponding FDTD simulation of the electric field intensity (V^2/m^2) in a cross-sectional plane from the center of particles. b) Bend loss as a function of bend radius measured at 1525 nm. c) SEM micrographs of 6 different fabricated 90° Huygens' meta-waveguide bends with bending radii of 2.7, 3.8, 5.4, 7.6, 10.3, and 21 μm. d) SEM micrograph of a power splitter incorporating Huygens' scatterers. The top inset shows the zoomed area of the splitting region while the right inset shows the simulated electric field intensity (V^2/m^2) in an in-plane cross section through the center of the particles. e) Transmittance spectra measured at one the arms of the splitter shown in (d). The transmittance of a standard silicon wire waveguide splitter is shown as a reference.

Finally, we have designed and fabricated waveguide power splitters based on arrangements of Huygens' scatterers. To this end, a Huygens' meta-waveguide was interconnected with a dimer consisting of two Huygens' scatterers with a 100 nm gap in between them. This choice of gap distance is dictated by fabrication constraints, light coupling efficiency to the dimer could be even higher for smaller gaps. The light coupled to the individual scatterers of the dimer was guided through a Huygens' meta-waveguide comprising 40 scatterers forming an S-bend. A SEM micrograph of the fabricated structure is shown in Figure 3d. The right inset of Figure 3d displays the simulated electric field intensity profile of the Huygens' meta-splitter while the top inset shows a close-up of the power-splitting region. The measured transmittance of the power splitter in one of the output waveguides is shown in Figure 3e. Our suggested design performs as well as conventional highly optimized power splitters[53] while yielding almost 5 times of size reduction. Using numerical calculations, we further demonstrated that the splitting ratio can be adjusted by displacement of the dimer with respect to the input waveguide (see Figure S2, Supporting Information). Altogether these results show that the forward scattering properties of Huygens' scatterers can also be harnessed to create highly compact and efficient integrated optical components.

4. Conclusion

In this work, we have numerically investigated and experimentally demonstrated a new type of CMOS-compatible on-chip optical waveguide operating in the telecom spectral range. Being inspired from concepts of optical metamaterials, in particular dielectric Huygens' metasurfaces, the demonstrated waveguide topologies are composed of judiciously engineered silicon nanoparticles and combine a Mie-resonant response with highly directional transmittance. The latter is achieved via tailoring the geometry of the individual nanoparticles, thus gaining control over their scattering properties. Specifically, by overlapping the dipolar electric and magnetic resonances of the nanoparticles, the resulting Huygens' scatterers exhibit strongly forward scattering characteristics as the Kerker condition of zero backward scattering is fulfilled over a broad spectral range. We demonstrated that the propagation loss through these Huygens' meta-waveguides is as low as 0.4 dB mm^{-1} along 18 000 coupled nanoparticles, exceeding the current record of 5.5 dB mm^{-1}[39] for Mie-resonant waveguides by more than an order of magnitude. The realized Huygens' meta-waveguides show a negative group index over a broad spectral region of 60 nm and over propagation distances of several millimeters, as well as regions of almost vanishing and

anomalous dispersion. Thus, they establish interesting regimes of light propagation at telecom wavelengths, opening up exciting new opportunities for research and applications in dispersion engineering,[38] ultrahigh bandwidth communications, as well as nonlinear and ultrafast nanophotonics.[42]

Moreover, the Huygens' meta-waveguides provide a practical platform to realize a range of compact and efficient integrated photonic components. In this work we have demonstrated two exemplary components, namely resonant protected waveguide bends and ultra compact power splitters, also confirming the natural ability of Huygens' waveguides to efficiently connect to other resonant nanophotonic components.

Altogether, our Huygens' meta-waveguides add new complementary capabilities to the toolbox of integrated photonics. Their unique waveguiding properties achieved by the control of light scattering at the level of the individual building blocks offer unprecedented opportunities for manipulating the flow of light on a silicon chip and for seamless integration of conventional on-chip waveguides with nanophotonic components such as nanoantennas, nanoresonators, and metasurfaces. The resonant response of the individual Huygens' scatterers has the potential for enhancing and tailoring light–matter interaction processes, such as light emission, absorption, and nonlinear optical phenomena. The Huygens' meta-waveguides can also be interesting for implementing new functionalities, such as miniaturized modulators, coupling of nanoscale emitters, dispersion-engineered nanophotonic devices and on-chip quantum optics. We believe that our results open excellent prospects for future implementations of Huygens' engineered waveguide devices in complex photonic architectures, ushering in a new field of resonant metamaterial integrated photonics.

5. Experimental Section

Device Fabrication: Samples were fabricated using a commercial foundry service, Applied Nanotools inc. Electron beam lithography was used on commercial silicon-on-insulator (SOI) substrates consisting of a 220-nm-thick layer of single-crystalline silicon and a 3-μm buried oxide (BOX) layer on top of a silicon handle wafer. Waveguide patterns were defined by electron beam lithography. The patterns were then transferred into the silicon layer by plasma etching. The samples were coated with a 3-μm SiO_2 cladding layer using plasma enhanced chemical vapor deposition (PECVD). Finally, a second lithographic step and etching was performed to define the optical facets used for coupling light into and out of the chip, first etching vertically through the upper oxide and BOX layers, and then into the silicon substrate. Finally, the chips were diced in proximity to the etched facets.

Measurement of Waveguide Propagation Loss and Transmittance Spectra: The light from a tunable continuous-wave semiconductor laser was coupled to a polarization-maintaining (PM) fiber. The input polarization was set to TE by a pigtailed half-wave plate polarization rotator. Lensed optical fibers with a Gaussian beam waist of 3 μm were utilized to couple light in and out of the waveguides using high-efficiency on-chip metamaterial couplers.[46] The output signal was collected by a microscope objective imaging the output aperture of each waveguide onto an InGaAs photodetector. An additional polarizer was used in the detection path to ensure only TE-polarized light reaches the detector. Data acquisition was synchronized with the tuning of the laser wavelength at wavelength resolution of 1 pm. The setup loss from the optical fiber and polarization optics was determined as 1.1 dB by a direct fiber-to-fiber calibration measurement with the chip removed. The mode propagation loss was determined by cut-back technique using Huygens' meta-waveguides of different lengths up to 7.78 mm corresponding to 18 000 nanoparticles.

Numerical Simulations of the Nanoparticle Scattering: To numerically investigate the scattering properties of the individual nanoparticles, the commercial finite-difference time-domain (FDTD) solver from Ansys/Lumerical was used. A single nanoparticle was placed in the center of the three-dimensional FDTD simulation domain. The structure was illuminated by a plane wave launched from a total-field scattered-field (TFSF) source positioned at a half-wavelength distance from the nanoparticle surface. The plane wave was linearly polarized along the *y*-axis (TE) and propagating along the *x*-axis (see coordinate system in Figure 1a). 10 monitors surrounding the nanoparticle were defined, allowing to divide the cubic simulation domain into forward- and backward-scattering regions. Perfectly matched layers were employed to absorb the scattered field. An automatic non-uniform mesh refinement, yielding convergence for a 5 nm mesh size near the nanoparticle surface was used. Scattering cross-sections were calculated by integrating the power detected at the monitors. The integrated power was normalized by the net input power and scattering surface area. The forward and backward scattering efficiencies were obtained by integrating only over the field power detected by the monitors situated within the forward and backward half-spaces, correspondingly, with respect to the center of the particle. The same procedure was used to calculate the forward to backward scattering ratio of the dimer (see Figure 1c). In this case, the forward and backward scattering regions at the center of the second particle were separated.

Dispersion Diagram and Bloch Modes: For the calculation of the dispersion diagram of the meta-waveguides (see Figure 1a for an illustration of the unit cell), periodic Bloch boundary conditions were applied in the propagation direction (*x*-axis) while PMLs were defined in the transverse directions. For all the simulations, the PMLs were positioned ≈1 wavelength away from the nanoparticle surface and a 5 nm mesh size was used near the nanoparticle. Ten randomly positioned broadband dipole sources and a TE polarized plane wave propagating in the *x*-direction were placed in order to excite all possible modes of the system. The normalized wave-vector in propagation direction was discretized equidistantly into 51 sample points between $k_x = 0$–0.5 $(2\pi/a)$. At frequencies where a guided mode (i.e., a band) exists, the fields couple to this mode and propagate indefinitely along the NP chain. At all other frequencies, the fields decay and vanish. The simulation time of 2000 fs to ensure the complete decay of the excitation and evanescent fields was set. Then the guided modes of the system were identified for each wavevector by recording the resonant frequencies of the fields that persist in the simulation using field monitors.

Multipolar Expansion: A multipolar expansion on induced field distribution of the single nanoparticle as well as 1D infinite array of nanoparticles was performed. In the literature, different formulations of the expansions exist based on the basis (spherical or Cartesian) or the considered physical quantity (scattered fields or induced currents). Here the formulation outlined in ref. [54] and implemented in ref. [55] for Cartesian coordinates and induced current densities was used. For single NPs, the standard procedure as described in the literature was employed. For the periodic Huygens' meta-waveguides, the method described in the previous section to extract the three-dimensional field distributions of the Bloch modes at 81 equidistantly spaced wavevector points between $k_x = 0.3$–0.5 $(2\pi/a)$ inside a unit-cell of the array was used. Three-dimensional field profiles at 251 wavelength points between 1200 and 1900 nm for each k_x was recorded. As there is only a single solution in a given branch for each k_x, this procedure yielded 162 distinct three-dimensional field profiles (eigenvectors) at 162 different wavelengths, i.e., 81 solutions for SWG branch and 81 for Huygens' branch. Standard multipolar expansion procedure was applied to all three-dimensional field profiles and the resulting multipolar expansion for each field profile was recorded. Note that this method was highly dependent on the sources inside the simulation domain as the procedure relied on the excitation of three-dimensional Bloch modes. Hence, the multipolar expansion of each branch with respect to corresponding ED magnitude in order to eliminate Bloch mode excitation dependencies was normalized.

Supporting Information

Supporting Information is available from the Wiley Online Library or from the author.

Acknowledgements

This project was funded by the Deutsche Forschungsgemeinschaft (DFG, German Research Foundation, project numbers 448835038, 437527638 (International Research Training Group (IRTG) 2675 'Meta-ACTIVE'), IRTG2101, and STA 142612-1) and by the State of Thuringia (Quantum Hub Thüringen, 2101 GFI 0043, Qi2.7). The authors also thank Dr. James Pond for his advice on the simulation of 1-D resonant NP arrays and Prof. Ulf Peschel for useful discussion. We are thankful to Dr. Shurui Wang for her help in the experimental characterizations.

Open access funding enabled and organized by Projekt DEAL.

Conflict of Interest

The authors declare no conflict of interest.

Data Availability Statement

The data that support the findings of this study are available from the corresponding author upon reasonable request.

Keywords

directional scattering, integrated photonics, meta-waveguides, negative group index, silicon photonics

Received: November 11, 2022
Revised: March 3, 2023
Published online: March 21, 2023

[1] A. H. Atabaki, S. Moazeni, F. Pavanello, H. Gevorgyan, J. Notaros, L. Alloatti, M. T. Wade, C. Sun, S. A. Kruger, H. Y. Meng, K. Al Qubaisi, I. Wang, B. H. Zhang, A. Khilo, C. V. Baiocco, M. A. Popovic, V. M. Stojanovic, R. J. Ram, *Nature* **2018**, *556*, 349.
[2] H. J. Caulfield, S. Dolev, *Nat. Photonics* **2010**, *4*, 261.
[3] H. S. Zhong, H. Wang, Y. H. Deng, M. C. Chen, L. C. Peng, Y. H. Luo, J. Qin, D. Wu, X. Ding, Y. Hu, P. Hu, X. Y. Yang, W. J. Zhang, H. Li, Y. X. Li, X. Jiang, L. Gan, G. W. Yang, L. X. You, Z. Wang, L. Li, N. L. Liu, C. Y. Lu, J. W. Pan, *Science* **2020**, *370*, 1460.
[4] J. W. Wang, F. Sciarrino, A. Laing, M. G. Thompson, *Nat. Photonics* **2020**, *14*, 273.
[5] W. Bogaerts, D. Perez, J. Capmany, D. A. B. Miller, J. Poon, D. Englund, F. Morichetti, A. Melloni, *Nature* **2020**, *586*, 207.
[6] Y. C. Shen, N. C. Harris, S. Skirlo, M. Prabhu, T. Baehr-Jones, M. Hochberg, X. Sun, S. J. Zhao, H. Larochelle, D. Englund, M. Soljacic, *Nat. Photonics* **2017**, *11*, 441.
[7] Y. Shi, Z. Li, P. Y. Liu, B. T. T. Nguyen, W. Wu, Q. Zhao, L. K. Chin, M. Wei, P. H. Yap, X. Zhou, H. Zhao, D. Yu, D. P. Tsai, A. Q. Liu, *Adv. Photonics Res.* **2021**, *2*, 2000150.
[8] A. Orieux, E. Diamanti, *J. Opt. (Bristol, U. K.)* **2016**, *18*, 083002.
[9] Y. Meng, Y. Z. Chen, L. H. Lu, Y. M. Ding, A. Cusano, J. A. Fan, Q. M. Hu, K. Y. Wang, Z. W. Xie, Z. T. Liu, Y. M. Yang, Q. Liu, M. L. Gong, Q. R. Xiao, S. L. Sun, M. M. Zhang, X. C. Yuan, X. J. Ni, *Light: Sci. Appl.* **2021**, *10*, 235.
[10] I. Staude, J. Schilling, *Nat. Photonics* **2017**, *11*, 274.
[11] S. Hughes, L. Ramunno, J. F. Young, J. E. Sipe, *Phys. Rev. Lett.* **2005**, *94*, 033903.
[12] P. Cheben, D. X. Xu, S. Janz, A. Densmore, *Opt. Express* **2006**, *14*, 4695.
[13] P. Cheben, P. J. Bock, J. H. Schmid, J. Lapointe, S. Janz, D. X. Xu, A. Densmore, A. Delage, B. Lamontagne, T. J. Hall, *Opt. Lett.* **2010**, *35*, 2526.
[14] J. M. Luque-Gonzalez, A. Sanchez-Postigo, A. Hadij-ElHouati, A. Ortega-Monux, J. G. Wanguemert-Perez, J. H. Schmid, P. Cheben, I. Molina-Fernandez, R. Halir, *Nanophotonics* **2021**, *10*, 2765.
[15] D. Urbonas, R. F. Mahrt, T. Stoferle, *Light: Sci. Appl.* **2021**, *10*, 15.
[16] C. M. Soukoulis, M. Wegener, *Science* **2010**, *330*, 1633.
[17] N. F. Yu, F. Capasso, *Nat. Mater.* **2014**, *13*, 139.
[18] Y. R. Fang, M. T. Sun, *Light: Sci. Appl.* **2015**, *4*, e294.
[19] a) R. Guo, M. Decker, F. Setzpfandt, X. Gai, D. Y. Choi, R. Kiselev, A. Chipouline, I. Staude, T. Pertsch, D. N. Neshev, Y. S. Kivshar, *Sci. Adv.* **2017**, *3*, e1700007; b) S. Saha, A. Dutta, N. Kinsey, A. V. Kildishev, V. M. Shalaev, A. Boltasseva, *ACS Photonics* **2018**, *5*, 4423.
[20] P. Cheben, R. Halir, J. H. Schmid, H. A. Atwater, D. R. Smith, *Nature* **2018**, *560*, 565.
[21] L. Ding, D. Eschimese, T. Y. L. Ang, D. Morits, H. S. Chu, S. T. Lim, C. E. Png, S. Gorelik, R. Paniagua-Dominguez, A. I. Kuznetsov, *ACS Appl. Nano Mater.* **2022**, *5*, 3170.
[22] A. E. Krasnok, A. E. Miroshnichenko, P. A. Belov, Y. S. Kivshar, *Opt. Express* **2012**, *20*, 20599.
[23] A. E. Krasnok, A. E. Miroshnichenko, P. A. Belov, Y. S. Kivshar, *JETP Lett.* **2011**, *94*, 593.
[24] D. Neshev, I. Aharonovich, *Light: Sci. Appl.* **2018**, *7*, 58.
[25] J. X. Zhou, H. L. Qian, C. F. Chen, J. X. Zhao, G. R. Li, Q. Y. Wu, H. L. Luo, S. C. Wen, Z. W. Liu, *Proc. Natl. Acad. Sci. U. S. A.* **2019**, *116*, 11137.
[26] S. Krasikov, A. Tranter, A. Bogdanov, Y. Kivshar, *Opto-Electron. Adv.* **2022**, *5*, 210147.
[27] K. Wang, J. G. Titchener, S. S. Kruk, L. Xu, H. P. Chung, M. Parry, I. I. Kravchenko, Y. H. Chen, A. S. Solntsev, Y. S. Kivshar, D. N. Neshev, A. A. Sukhorukov, *Science* **2018**, *361*, 1104.
[28] S. Q. Li, X. W. Xu, R. M. Veetil, V. Valuckas, R. Paniagua-Dominguez, A. I. Kuznetsov, *Science* **2019**, *364*, 1087.
[29] S. T. Ha, Y. H. Fu, N. K. Emani, Z. Y. Pan, R. M. Bakker, R. Paniagua-Dominguez, A. I. Kuznetsov, *Nat. Nanotechnol.* **2018**, *13*, 1042.
[30] C. J. Zou, A. Komar, S. Fasold, J. Bohn, A. A. Muravsky, A. A. Murauski, T. Pertsch, D. N. Neshev, I. Staude, *ACS Photonics* **2019**, *6*, 1533.
[31] T. Santiago-Cruz, A. Fedotova, V. Sultanov, M. A. Weissflog, D. Arslan, M. Younesi, T. Pertsch, I. Staude, F. Setzpfandt, M. Chekhova, *Nano Lett.* **2021**, *21*, 4423.
[32] A. Tittl, A. Leitis, M. K. Liu, F. Yesilkoy, D. Y. Choi, D. N. Neshev, Y. S. Kivshar, H. Altug, *Science* **2018**, *360*, 1105.
[33] J. J. Du, S. Y. Liu, Z. F. Lin, J. Zi, S. T. Chui, *Phys. Rev. A* **2011**, *83*, 035803.
[34] G. S. Blaustein, M. I. Gozman, O. Samoylova, I. Y. Polishchuk, A. L. Burin, *Opt. Express* **2007**, *15*, 17380.
[35] R. S. Savelev, D. S. Filonov, P. V. Kapitanova, A. E. Krasnok, A. E. Miroshnichenko, P. A. Belov, Y. S. Kivshar, *Appl. Phys. Lett.* **2014**, *105*, 181116.
[36] R. S. Savelev, A. P. Slobozhanyuk, A. E. Miroshnichenko, Y. S. Kivshar, P. A. Belov, *Phys. Rev. B* **2014**, *89*, 035435.
[37] R. S. Savelev, D. S. Filonov, M. I. Petrov, A. E. Krasnok, P. A. Belov, Y. S. Kivshar, *Phys. Rev. B* **2015**, *92*, 155415.
[38] R. S. Savelev, A. V. Yulin, A. E. Krasnok, Y. S. Kivshar, *ACS Photonics* **2016**, *3*, 1869.
[39] R. M. Bakker, Y. F. Yu, R. Paniagua-Domínguez, B. Luk'Yanchuk, A. I. Kuznetsov, *Nano Lett.* **2017**, *17*, 3458.

[40] T. X. Hoang, S. T. Ha, Z. Y. Pan, W. K. Phua, R. Paniagua-Dominguez, C. E. Png, H. S. Chu, A. I. Kuznetsov, *Nano Lett.* **2020**, *20*, 5655.
[41] F. H. Viktoriia Rutckaia, G. Schmidt, A. Novikov, M. Shaleev, R. Savelev, J. Schilling, M. Petrov, *arXiv:2006.13185*, **2020**.
[42] M. Decker, I. Staude, M. Falkner, J. Dominguez, D. N. Neshev, I. Brener, T. Pertsch, Y. S. Kivshar, *Adv. Opt. Mater.* **2015**, *3*, 813.
[43] M. Kerker, D. S. Wang, C. L. Giles, *J. Opt. Soc. Am.* **1983**, *73*, 765.
[44] R. Alaee, R. Filter, D. Lehr, F. Lederer, C. Rockstuhl, *Opt. Lett.* **2015**, *40*, 2645.
[45] C. F. Bohren, D. R. Huffman, *Absorption and Scattering of Light by Small Particles*, John Wiley & Sons, Hoboken, NJ **2008**.
[46] P. Cheben, J. H. Schmid, S. R. Wang, D. X. Xu, M. Vachon, S. Janz, J. Lapointe, Y. Painchaud, M. J. Picard, *Opt. Express* **2015**, *23*, 22553.
[47] L. Ding, Y. F. Yu, D. Morits, M. B. Yu, T. Y. L. Ang, H. S. Chu, S. T. Lim, C. E. Png, R. Paniagua-Dominguez, A. I. Kuznetsov, *Nanoscale* **2020**, *12*, 21713.
[48] L. Chrostowski, M. Hochberg, *Silicon Photonics Design: From Devices to Systems*, Cambridge University Press, Cambridge **2015**.
[49] L. J. Wang, A. Kuzmich, A. Dogariu, *Nature* **2000**, *406*, 277.
[50] R. W. Boyd, *J. Mod. Optic.* **2009**, *56*, 1908.
[51] H. P. Uranus, H. J. W. M. Hoekstra, *J. Lightwave Technol.* **2007**, *25*, 2376.
[52] M. Bahadori, M. Nikdast, Q. X. Cheng, K. Bergman, *J. Lightwave Technol.* **2019**, *37*, 3044.
[53] Y. Zhang, S. Y. Yang, A. E. J. Lim, G. Q. Lo, C. Galland, T. Baehr-Jones, M. Hochberg, *Opt. Express* **2013**, *21*, 1310.
[54] R. Alaee, C. Rockstuhl, I. Fernandez-Corbaton, *Opt. Commun.* **2018**, *407*, 17.
[55] T. Hinamoto, M. Fujii, *OSA Continuum* **2021**, *4*, 1640.